

Forward Shock Proper Motions of Kepler's Supernova Remnant

S. Katsuda¹, H. Tsunemi¹, H. Uchida¹, and M. Kimura¹

ABSTRACT

The X-ray structure of Kepler's supernova remnant shows a rounded shape delineated by forward shocks. We measure proper-motions of the forward shocks on overall rims of the remnant, by using archival *Chandra* data taken in two epochs with time difference of 6.09 yr. The proper-motions of the forward shocks on the northern rim are measured to be $0''.076 (\pm 0''.032 \pm 0''.016) - 0''.11 (\pm 0''.014 \pm 0''.016) \text{ yr}^{-1}$, while those on the rest of the rims are measured to be $0''.15 (\pm 0''.017 \pm 0''.016) - 0''.30 (\pm 0''.048 \pm 0''.016) \text{ yr}^{-1}$, here the first-term errors are statistical uncertainties and the second-term errors are systematic uncertainties. Combining the best-estimated shock velocity of $1660 \pm 120 \text{ km sec}^{-1}$ measured for Balmer-dominated filaments in the northern and central portions of the remnant (Sankrit et al. 2005) with the proper-motions derived for the forward shocks on the northern rim, we estimate the distance of $3.3_{-0.4}^{+1.6} \text{ kpc}$ to the remnant. We measure the expansion indices, m , (defined as $R \propto t^m$) to be 0.47–0.82 for most of the rims. These values are consistent with those expected in Type-Ia SN explosion models, in which the ejecta and the circumstellar medium have power-law density profiles whose indices are 5–7 and 0–2, respectively. Also, we should note the slower expansion on the northern rim than that on the southern rim. This is likely caused by the inhomogeneous circumstellar medium; the density of the circumstellar medium is higher in the north than that in the south of the remnant. The newly estimated geometric center, around which we believe the explosion point exists, is located at $\sim 5''$ offset in the north of the radio center.

Subject headings: ISM: individual (Kepler's Supernova) — shock waves — supernova remnants — X-rays: ISM

1. Introduction

Kepler's supernova remnant (SNR; SN 1604) is one of the historical SNRs. The X-ray structure of the remnant shows a clear circular shape with a radius of about $100''$. The

¹Department of Earth and Space Science, Graduate School of Science, Osaka University, 1-1 Machikaneyama, Toyonaka, Osaka, 560-0043, Japan; katsuda@ess.sci.osaka-u.ac.jp

distance estimations to the remnant have been scattered in a range of 3–5 kpc (e.g., Green 1984; Schaefer 1994). Although the far side of 5 kpc supported by H I observations (Reynoso & Goss 1999) has been adopted in recent literature, optical studies combining proper-motions with shock velocities of Balmer-dominated filaments have preferred a near side of 2.9 ± 0.4 kpc (Blair et al. 1991) or $3.9^{+1.4}_{-0.9}$ kpc (Sankrit et al. 2005).

The SN type of Kepler’s SNR is very interesting. Based on the light curve of the Kepler’s SN, Baade (1943) classified this remnant as a result of Type-Ia SN. *Ginga* spectrum from this remnant showed a strong Fe K line, supporting that the Kepler’s SN was a Type-Ia SN (Hatsukade et al. 1990). *ASCA* spectrum of this remnant showed strong K-shell lines from Si, S, and Fe, and the measured relative abundances supported Type-Ia origin (Kinugasa & Tsunemi 1999). Recent deep *Chandra* observations detected strong emission lines from heavy elements almost everywhere in the remnant, again supporting Type-Ia origin (Reynolds et al. 2007). On the other hand, the density of the ambient medium around the remnant was estimated to be so high (at least 1 cm^{-3} ; e.g., Hughes & Helfand 1985) at a large height of ~ 470 pc (assuming the distance of 4 kpc to the remnant) from the Galactic plane. The high density of the ambient medium was considered to be a signature of circumstellar material (CSM) which was blown off from a progenitor star as a stellar wind. In addition to the existence of the dense surroundings, Nitrogen-rich materials as a result of CNO-processing in a massive progenitor star were detected in some optical knots (van den Bergh & Kamper 1977; Dennefeld 1982). These facts suggested that the Kepler’s remnant was core-collapse in origin. Also, Bandiera (1987) suggested a massive runaway star as a possible progenitor of Kepler’s SNR, since it was able to naturally account for the presence of the CSM and the asymmetric structure of the remnant in optical wavelength. Recently, Blair et al. (2007) proposed that the Kepler’s SN was categorized as a Type-Ia explosion in a region with significant CSM, which was a small but growing class of Type-Ia SNe named as Type-Ia/IIn by Kotak et al. (2004). Due to the large expansion of Kepler’s SNR, it is the best target from which we can investigate the detailed preexisting structures of the CSM for this rare kind of SNe.

Here, we report proper-motions of the forward shocks on the overall rims of Kepler’s SNR, by using archival *Chandra* data. We derive the distance to the remnant, combining the proper-motions we measure with the optically determined forward shock velocity (Sankrit et al. 2005). Also, we present evolutionary states in various portions of the remnant, which gives us critical information on structures of the surrounding CSM.

2. Observations

Kepler’s SNR was observed on three epochs in 2000 (PI: Holt, S.), 2004 (PI: Rudnick, L.), and 2006 (PI: Reynolds, S.). We use the first (ObsID. 116) and the last (ObsID. 6715) observation to measure proper-motions of the forward shocks of this remnant. These observations were, respectively, done in June 30th 2000 and August 4–6th 2006, resulting in the time difference of 6.09 yr. The entire remnant was covered on the ACIS-S3 back-illuminated chip in both observations. We start our analysis from level 2 event files processed with calibration data files in CALDB ver. 3.4.0 for ObsID. 116, ver. 3.2.2 for ObsID. 6715. We exclude the high-background periods for data from ObsID. 116, whereas there seems no significant background flares for the data from ObsID. 6715 so that we reject no data from the level 2 event file for this data set. The resulting net exposure times for ObsID. 116 and 6715 are 37.8 ks and 159.1 ks, respectively.

To measure proper-motions of the forward shocks, we use an energy range of 1.0–8.0 keV, i.e., we do not use an energy range below 1.0 keV where building up contaminants on the detector significantly reduce count rates for the second-epoch observation. Figure 1 *left* shows the second-epoch image of the entire Kepler’s SNR in the energy range of 1.0–8.0 keV.

3. Analysis and Results

We register the two images by aligning them on four point sources that are obviously seen in the vicinity of the remnant. We determine the positions of the four sources in both observations, employing `wavdetect` software included in CIAO ver. 3.4. We find a systematic offset between the two images; the sense of the difference is that the first-epoch image is south and west of the second. We calculate the error-weighted mean offset of the four point sources to be $0''.14$ in right ascension and $0''.19$ in declination. Then, the first-epoch image is shifted in right ascension by $0''.14$ and in declination by $0''.19$ with respect to the second-epoch image. Once the two images are registered, we do not need to consider the absolute astrometric uncertainty of $0''.6$ reported by the *Chandra* calibration team as systematic errors in our analysis. We take account of $0''.1$, i.e., the relative astrometric uncertainty reported by the *Chandra* calibration team, as systematic errors in the following proper-motion measurements.

Figure 1 *right* shows a difference image between two epochs after being registered and normalized to match the count rates in the two epochs. We clearly see a signature of the expansion as positive emission (seen as white in the figure) with negative emission (seen as black in the figure). Note that the horizontal stripes seen in the northern rim of the remnant

are due to bad columns on the ACIS-S3 chip.

To measure proper-motions of the forward shocks of the remnant, we focus on 14 rectangular regions at the edge of the X-ray image (see, Fig. 1 *left*). We then project the image into one dimension so that we generate one-dimensional profile along perpendicular direction to the shock motion (hereafter, radial profile). Each bin of the radial profile is spaced by $0''.25$. We adjust the position angle for each rectangular region as tangential as possible to the shock front in the following way. We generate radial profiles for position angle with trial angles of 2° steps. For each trial position angle, we calculate

$$I = \sum_i I_i^2,$$

where I_i is the intensity in each bin, i . The position angle with the largest value of I represents the most tangential angle to the shock front. The 14 regions with the “best” position angles are shown in Fig. 1 *left*. We plot example radial profiles from Reg-4 and Reg-14 in Fig. 2, from which we can see apparent shifts between the two epochs. To quantitatively measure the shifts, the first-epoch profile is shifted in radius with respect to the second-epoch profile, and χ^2 is calculated from the difference between the two profiles at each shift position (e.g., Katsuda et al. 2008). In this way, we obtain χ^2 profiles as a function of shift positions. By applying a quadratic function for the χ^2 profile, we measure the best-shift position where the minimum χ^2 -value (χ_{\min}^2) occurs. 90% statistical uncertainties on the best-shift are calculated using a criteria of $\chi_{\min}^2 + 2.7$. Table. 1 summarizes the best-shift positions between the two observations, χ_{\min}^2 per degrees of freedom, and proper motions for all the regions indicated in Fig. 1 *left*. The azimuthal angle for each region, which is measured counterclockwisely from the radio center at $\alpha = 17^{\text{h}}30^{\text{m}}41^{\text{s}}.5$, $\delta = -21^\circ29'23''$ (J2000; Matsui et al. 1984), is also listed in the table.

We find that the proper-motions vary from location to location. Plotting the proper-motion derived in each region as a function of azimuthal angle in Fig. 3, we find a trend that the proper-motions derived in the northern regions (i.e., Regs-1, 2, 13, and 14) are slower than those derived in the rest of the regions.

4. Discussion

4.1. Distance to the Remnant

We have measured proper-motions of the forward shocks on overall rims of Kepler’s SNR. If we combine them with the shock velocities, the distance to the remnant can be determined. The velocities of the forward shocks associated with Balmer-dominated filaments, which were

located at the northern rim and the central portion of the remnant, were determined to be $1670\text{--}2800\text{ km sec}^{-1}$ (Fesen et al. 1989) or $1550\text{--}2000\text{ km sec}^{-1}$ (Blair et al. 1991) from their $\text{H}\alpha$ emission line widths. Under the assumption of little or no temperature equilibration between electrons and protons, Sankrit et al. (2005) determined the best-estimated shock velocity to be $1660\pm120\text{ km sec}^{-1}$. Since the best-estimated shock velocity represents the average velocity of the forward shocks with Balmer-dominated filaments seen in the northern and the central portion of the remnant, we should combine it with an error-weighted mean proper-motion measured in the northern regions (i.e., Regs-1, 2, 13, 14). Then, the best-estimated distance to the remnant is determined to be $3.3 (v/1660\text{ km sec}^{-1})(\mu/0''.107\text{ yr}^{-1})^{-1}\text{ kpc}$. We can estimate a distance range of $2.9\text{--}4.9\text{ kpc}$ to the remnant, considering the variation of the proper-motions derived in the four northern regions of $0''.076\text{--}0''.11\text{ yr}^{-1}$ as well as the uncertainty of the shock velocity. While the best-estimated distance determined here is less than $\sim 5\text{ kpc}$ (Reynoso & Goss 1999), it is well within the values previously measured based on the combination of the proper-motion and the shock-velocity of the Balmer-dominated filaments: from 2.9 kpc (Blair et al. 1991) to 3.9 kpc (Sankrit et al. 2005).

4.2. Asymmetry of the Forward Shock Velocity

We find velocity asymmetries of the forward shocks of Kepler’s SNR: shock velocities on the northern rim are 1.5–3 times slower than those on the other rims. If we assume the pressure equilibrium in the remnant, the velocity contrast of 1.5–3 requires a density contrast of $\sim 2\text{--}9$. Recently, Blair et al. (2007) estimated that the preshock density in the north of the remnant is $\sim 4\text{--}9$ times higher than that in the south, based on brightness variations observed between the northern and southern rims of the remnant at $24\text{ }\mu\text{m}$. Therefore, the slower expansion observed on the northern rim than those on the rest of the rims seems to be well explained by the density contrast suggested from the observation at $24\text{ }\mu\text{m}$.

It is interesting that Kepler’s SNR appears quite round in spite of the asymmetric velocities of the forward shocks. One possibility to explain this feature is that the forward shock encountered a dense gas on the northern rim so recently that we can hardly see apparent deceleration of the shock from morphological point of view. However, there have been no reports of such a very recent shock deceleration so far. (In addition, we can not obtain at least strong evidence that the forward shock on the northwestern rim shows recent significant deceleration; Sankrit et al. [2005] measured a proper-motion of a Balmer-dominated filament positionally coincident with the forward shock in Reg-13 from observations performed on two epochs in 1987 and 2003 to be $0''.089\pm0''.009\text{ yr}^{-1}$ that is consistent with

our estimation of the proper-motion of $0''.076 [\pm 0''.032 \pm 0''.016] \text{ yr}^{-1}$ determined in between 2000 and 2006). We propose another possibility that the expansion center of the remnant is located at a relatively northern position compared to the geometric center determined by the entire remnant. In fact, the outer edges of the X-ray structure seem to be outlined by two (ideally concentric) circles whose centers are located at the north of the radio center: one with a relatively small radius outlines the northern-half edge of the remnant, whereas the other with a relatively large radius outlines the southern-half edge. We estimate the best-fit circle for either the northern-half edge or the southern-half edge independently. Here, we define the northern half in a range of azimuthal angles from -50° (or 310°) to 45° , whereas the southern half in a range of azimuthal angles from 95° to 258° , such that the northern half covers the regions with proper-motions of $\sim 0''.1 \text{ yr}^{-1}$, whereas the southern half covers the other regions with proper-motions of above $\sim 0''.2 \text{ yr}^{-1}$. We define the edge of the X-ray extent (hereafter, X-ray boundary) as contours of 5 counts per $0''.492$ -sided pixel in the second-epoch 0.3–8.0 keV band image. We ignore X-ray boundaries showing apparent deviations from circular curvatures, in order not to yield misleading geometric centers and radii. The X-ray boundaries used to estimate the best-fit circles are drawn by white curves (contours) in Fig. 5. Assuming the geometric center, we calculate the distance, R_i , between each pixel, i , on the X-ray boundaries and the geometric center. For various trial geometric centers, we calculate

$$K = \sum_i (R - R_i)^2,$$

where R is a variable parameter representing a radius. We can derive the best-fit radius, R , as well as the geometric center at the minimum of the K -value. The best-fit circles representing the X-ray boundaries for the northern and southern halves are centered at $\alpha = 17^{\text{h}}30^{\text{m}}41^{\text{s}}.4$, $\delta = -21^\circ29'19''$ (J2000) with a radius of $93''$, and at $\alpha = 17^{\text{h}}30^{\text{m}}41^{\text{s}}.9$, $\delta = -21^\circ29'16''$ (J2000) with a radius of $120''$, respectively. Parts of these two circles are indicated in Fig. 5 as white dashed pie. We see that both geometric centers estimated are shifted by about $5''$ toward the north of the remnant from the radio center (see, Fig. 5), which results in a smaller radius for the circle representing the northern-half X-ray boundary than that for the southern-half X-ray boundary; the ratio of the radius is derived to be about 3:4. Although we cannot derive uncertainties on the center positions and radii in the least square method used above, we might estimate uncertainties on these parameters from the χ^2 method by introducing fake errors on the data (R_i). We introduce the fake errors of 1 % for the northern half and 3.5 % for the southern half, respectively, so that we can derive the reduced χ^2 -value of ~ 1 . The 90% uncertainties, i.e., $\chi^2 < \chi^2_{\text{min}} + 6.25$ as appropriate for three interesting parameters, are estimated to be $\pm 0''.5$ or $\pm 1''.5$ (in right ascension), and $\pm 1''.5$ or $\pm 2''$ (in declination) for the northern or southern halves, respectively. Therefore, the derived offset of $\sim 5''$ from the radio center seems to be significant, although we cannot strongly state the

significance without knowing the uncertainty of the radio center. Hydrodynamic simulations of a remnant expanding into a medium with a density gradient (Dohm-Palmer & Jones 1996) show that the shock outline remains roughly circular, while the center of the best-fit curvature can move away from the true explosion location by as much as 10 – 15% of the remnant radius. The offsets between geometric centers estimated here and the radio center (Matsui et al. 1984) are roughly 5% of the radius. Therefore, from theoretical point of view, our newly determined geometric centers can be possible true explosion locations of Kepler’s SNR. We believe that the true explosion point is around the geometric centers estimated here.

We consider the expansion center of Kepler’s SNR at $\alpha = 17^{\text{h}}30^{\text{m}}41^{\text{s}}.6$, $\delta = -21^{\circ}29'17''$ (J2000) that is the center point between the two center points of the circles representing the northern-half and southern-half X-ray boundaries. Then, the expansion rate can be calculated by dividing the proper-motion value in each region by the distance between the shock front and the expansion center. Combined with the age of the remnant of 400 yr, the expansion index, m , is also calculated, where the expansion of the forward shock of SNRs can be expressed as $R \propto t^m$ (i.e., the remnant’s radius is assumed to evolve as a power law with age; see, e.g., Woltjer 1972). Table. 2 summarizes these parameters and Fig. 4 shows the expansion indices as a function of azimuthal angle. SNRs cease being in pure free expansion ($m = 1$) after a few years, as they interact with circumstellar or interstellar gas. Then, a reverse shock into the ejecta is formed, and remnants evolve in what is usually called an ejecta-driven phase. In spherical symmetry, if both the ejecta and the CSM have power-law density profiles characterized by $\rho \propto r^{-n}$ and $\rho \propto r^{-s}$, respectively, the evolution becomes self-similar and is given by $R \propto t^{(n-3)/(n-s)}$, i.e., the expansion index, m , can be written as $(n - 3)/(n - s)$ (e.g., Chevalier 1982). Here, the value of s is 0 for a uniform CSM, and is 2 for a constant wind velocity from the progenitor star. In general, the s -value is expected to be 2 for core-collapse SNe, since massive stars which results in core-collapse SNe produce stellar wind before SN explosions, while both $s = 0$ and $s = 2$ can happen for Type-Ia SNe as mentioned in Section 1. As for n -values, $9 \lesssim n \lesssim 12$ is expected for a core-collapse origin (e.g., Chevalier 1992), while $5 \lesssim n \lesssim 7$ for a Type-Ia origin (e.g., Chevalier 1982). Therefore, for core-collapse SNe, the value of m is expected to be greater than $6/7$ ($=0.86$). On the other hand, for Type-Ia SNe, the value of m ranges from 0.4 to 0.8. Our measured m -values at all regions except for regions 6 and 13 range from 0.47 to 0.82, which is consistent with that expected from Type-Ia SNe. We find significant variations of m -values in this remnant, which suggests complicated CSM structures around the remnant. It should be remarked that the northern rim shows slower expansions than the southern rim does. The north-south density asymmetry of the CSM suggested from variations of surface brightness results in the variation of m -values between the northern rim and the southern rim.

It is worth noting how the velocity difference of the forward shock affects spectral features. As already noticed by *XMM-Newton* (Cassam-Chenaï et al. 2004) and *Chandra* (Reynolds et al. 2007) observations, a spectrum extracted around Reg-6 on the southeastern rim is non-thermal (synchrotron) in origin, whereas a spectrum around Reg-13 on the north-western rim is thermal in origin. We can clearly see the spectral difference in Fig. 6. This is considered as a result that the faster shock (4700 km sec^{-1} at a distance of 3.3 kpc) as well as the lower ambient density suggested by lower surface brightness in Reg-6 produces the synchrotron emission more efficiently than the slower (1200 km sec^{-1} at a distance of 3.3 kpc) shock as well as higher ambient density in Reg-13 does.

We should note previous X-ray expansion measurements based on *Einstein* and *ROSAT* observations performed by Hughes (1999). The mean expansion rates in the entire remnant was derived to be $\sim 0.24\% \text{ yr}^{-1}$. This value is larger than that estimated in our analysis; only one region (Reg-6) shows such a rapid expansion. Furthermore, he measured expansion rates as a function of azimuthal angle, by comparing long radial profiles from the geometric center to the X-ray boundaries between two *ROSAT* HRI observations. The expansion rates measured in the northern portion of the remnant did not show lower values than those in the other portions. This also conflicts to our results. These discrepancies might come from the different method between Hughes (1999) and this work. Hughes (1999) measured radially averaged proper-motions of the remnant, on the other hand, we measure proper-motions for the very edge of the remnant, i.e., the forward shocks themselves. Therefore, the faster expansion rates derived in Hughes (1999) than those in this work suggests that plasmas in the inner remnant show larger expansion rates than those of the forward shocks. Such a situation might indicate recent rapid deceleration of the forward shocks. However, as mentioned above, we have not yet observed (at least strong) such indications so far. Further detailed proper-motion measurements in the inner remnant are strongly required to reveal the reason of the discrepancies between the expansion rate by Hughes (1999) and that in this work.

5. Conclusions

We have measured proper-motions of the forward shocks on the overall rims of Kepler’s SNR, using the archival *Chandra* data.

The expansion indices measured at various parts of the rim supports the Type-Ia SN which has the situation that the ejecta and the CSM, respectively, have power-law density profiles with indices of 5–7 and 0–2 rather than the core-collapse SN.

We find that the shock velocities are asymmetric: the shock velocities on the northern rim are 1.5–3 times slower than those on the rest of the remnant. We attribute this asymmetry to the density inhomogeneities of the CSM surrounding the remnant. The shape of the X-ray boundary of the remnant as well as the inhomogeneous CSM structures lead us to consider that the expansion center is located at $\sim 5''$ offset in the north of the radio center.

This work is partly supported by a Grant-in-Aid for Scientific Research by the Ministry of Education, Culture, Sports, Science and Technology (16002004). S.K. is supported by JSPS Research Fellowship for Young Scientists.

REFERENCES

- Baade, W. 1943, ApJ, 97, 119
- Bandiera, R. 1987, ApJ, 319, 885
- Blair, W. P., Long, K. S., & Vancura, O. 1991, ApJ, 366, 484
- Blair, W. P., et al. 2007, ApJ, 662, 998
- Chevalier, R. A. 1982, ApJ, 259, L85
- Chevalier, R. A. 1992, ApJ, 394, 599
- Dohm-Palmer, R. C., & Jones, T. W. 1996, ApJ, 471, 279
- Cassam-Chenaï, G., Decourchelle, A., Ballet, J., Hwang, U., Hughes, J. P., & Petre, R. 2004, A&A, 414, 545
- Dennefeld, M. 1982, A&A, 112, 215
- Dickel, J. R., Sault, R., Arendt, R. G., Korista, K. T., & Matsui, Y. 1988, ApJ, 330, 254
- Fesen, R. A., Becker, R. H., Blair, W. P., & Long, K. S. 1989, ApJ, 338, L13
- Green, D. A., 1984, MNRAS, 209, 449
- Hatsukade, I., Tsunemi, H., Yamashita, K., Koyama, K., Asaoka, Y., & Asaoka, I. 1990, PASJ, 42, 279
- Hughes, J. P., & Helfand, D. J., 1985, ApJ, 291, 544
- Hughes, J. P. 1999, ApJ, 527, 298
- Katsuda, S., Tsunemi, H., Mori, K. ApJ, 678, L35
- Kinugasa, K., & Tsunemi, H. 1999, PASJ, 51, 239
- Kotak, R., Meikle, W. P. S., Adamson, A., & Leggett, S. K. 2004, MNRAS, 354, L13
- Matsui, Y., Long, K. S., Dickel, J. R., & Greisen, E. W. 1984, ApJ, 287, 295
- Reynolds, S. P., et al. 2007, ApJ, 668, L135
- Reynoso, E. M., & Goss, W. M. 1999, AJ, 118, 926

Sankrit, R., Blair, W. P., Delaney, T., Rudnick, L., Harrus, I. M., & Ennis, J. A. 2005, *Adv. Space Res.* 35, 1027

Schaefer, B. E. 1994, *ApJ*, 426, 493

van den Bergh, S., & Kamper, K. W. 1977, *ApJ*, 218, 617

Woltjer, L. 1972, *ARA&A*, 10, 129

Table 1. Summary of Proper-Motion Measurements

Region	Azimuth (deg)	$\chi^2_{\min}/\text{d.o.f.}$	Shift between the two epochs (arcsec)	Proper motion (arcsec yr ⁻¹)
Reg-1	16	1.68	0.63 ($\pm 0.09 \pm 0.10$)	0.109 ($\pm 0.013 \pm 0.016$)
Reg-2	32	0.54	0.66 ($\pm 0.08 \pm 0.10$)	0.104 ($\pm 0.015 \pm 0.016$)
Reg-3	75	0.85	0.91 ($\pm 0.11 \pm 0.10$)	0.149 ($\pm 0.017 \pm 0.016$)
Reg-4	96	1.47	1.16 ($\pm 0.09 \pm 0.10$)	0.191 ($\pm 0.015 \pm 0.016$)
Reg-5	102	2.27	1.26 ($\pm 0.10 \pm 0.10$)	0.206 ($\pm 0.016 \pm 0.016$)
Reg-6	135	1.56	1.84 ($\pm 0.29 \pm 0.10$)	0.302 ($\pm 0.048 \pm 0.016$)
Reg-7	155	1.71	1.08 ($\pm 0.18 \pm 0.10$)	0.178 ($\pm 0.030 \pm 0.016$)
Reg-8	172	1.39	1.48 ($\pm 0.16 \pm 0.10$)	0.242 ($\pm 0.025 \pm 0.016$)
Reg-9	230	1.80	1.25 ($\pm 0.13 \pm 0.10$)	0.206 ($\pm 0.021 \pm 0.016$)
Reg-10	242	1.00	0.99 ($\pm 0.13 \pm 0.10$)	0.162 ($\pm 0.022 \pm 0.016$)
Reg-11	250	1.25	1.29 ($\pm 0.24 \pm 0.10$)	0.212 ($\pm 0.040 \pm 0.016$)
Reg-12	258	1.06	1.10 ($\pm 0.17 \pm 0.10$)	0.180 ($\pm 0.027 \pm 0.016$)
Reg-13	319	0.89	0.46 ($\pm 0.19 \pm 0.10$)	0.076 ($\pm 0.032 \pm 0.016$)
Reg-14	345	1.06	0.70 ($\pm 0.08 \pm 0.10$)	0.114 ($\pm 0.014 \pm 0.016$)

Note. — First-term errors represent 90% statistical uncertainties and second-terms errors represent systematic uncertainties.

Table 2. Summary of Expansion Rates and Expansion Indices

Region	Azimuth (deg)	Exapnsion Rate (%)	X-Ray Expansion Index	Radio Expansion Index ^a
Reg-1	16	0.12 ($\pm 0.01 \pm 0.02$)	0.49 ($\pm 0.06 \pm 0.07$)	0.45
Reg-2	32	0.12 ($\pm 0.02 \pm 0.02$)	0.47 ($\pm 0.07 \pm 0.07$)	0.45
Reg-3	75	0.16 ($\pm 0.02 \pm 0.02$)	0.63 ($\pm 0.07 \pm 0.07$)	0.65
Reg-4	96	0.17 ($\pm 0.01 \pm 0.01$)	0.68 ($\pm 0.05 \pm 0.06$)	—
Reg-5	102	0.17 ($\pm 0.01 \pm 0.01$)	0.70 ($\pm 0.05 \pm 0.05$)	—
Reg-6	135	0.25 ($\pm 0.04 \pm 0.01$)	0.98 ($\pm 0.16 \pm 0.05$)	—
Reg-7	155	0.16 ($\pm 0.03 \pm 0.01$)	0.63 ($\pm 0.11 \pm 0.06$)	—
Reg-8	172	0.20 ($\pm 0.02 \pm 0.01$)	0.82 ($\pm 0.08 \pm 0.05$)	—
Reg-9	230	0.18 ($\pm 0.02 \pm 0.01$)	0.71 ($\pm 0.07 \pm 0.06$)	—
Reg-10	242	0.14 ($\pm 0.02 \pm 0.01$)	0.55 ($\pm 0.08 \pm 0.06$)	0.55
Reg-11	250	0.18 ($\pm 0.03 \pm 0.01$)	0.72 ($\pm 0.14 \pm 0.05$)	0.55
Reg-12	258	0.16 ($\pm 0.02 \pm 0.01$)	0.62 ($\pm 0.09 \pm 0.06$)	0.55
Reg-13	319	0.08 ($\pm 0.04 \pm 0.02$)	0.34 ($\pm 0.14 \pm 0.07$)	0.35
Reg-14	345	0.12 ($\pm 0.02 \pm 0.02$)	0.50 ($\pm 0.06 \pm 0.07$)	0.35

Note. — First-term errors represent 90% statistical uncertainties and second-term errors represent systematic uncertainties. ^aDickel et al. (1988) without particulary uncertain data.

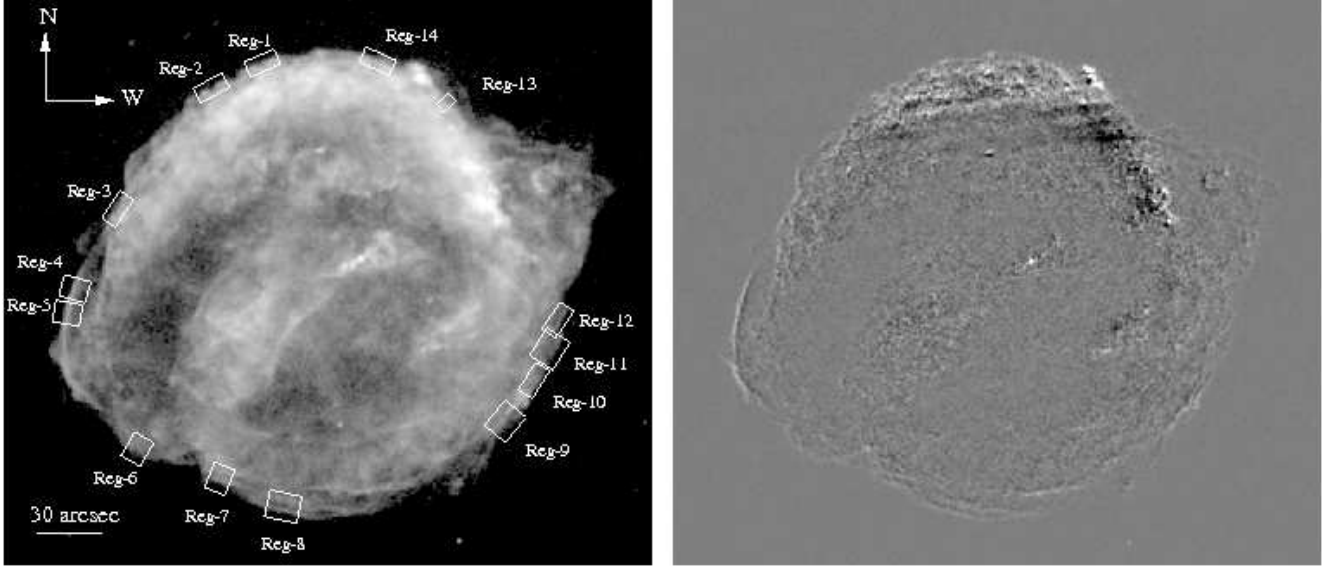


Fig. 1.— *Left*: *Chandra* 1.0–8.0 keV band image obtained in the second-epoch observation. The image is binned by $0''.492$ and has been smoothed by Gaussian kernel of $\sigma = 0''.984$. The intensity scale is logarithmic. We measure proper-motions of the forward shock in 14 regions indicated as rectangles (from Reg-1 to Reg-14). *Right*: Linearly scaled difference (2006–2000) image between the two epochs.

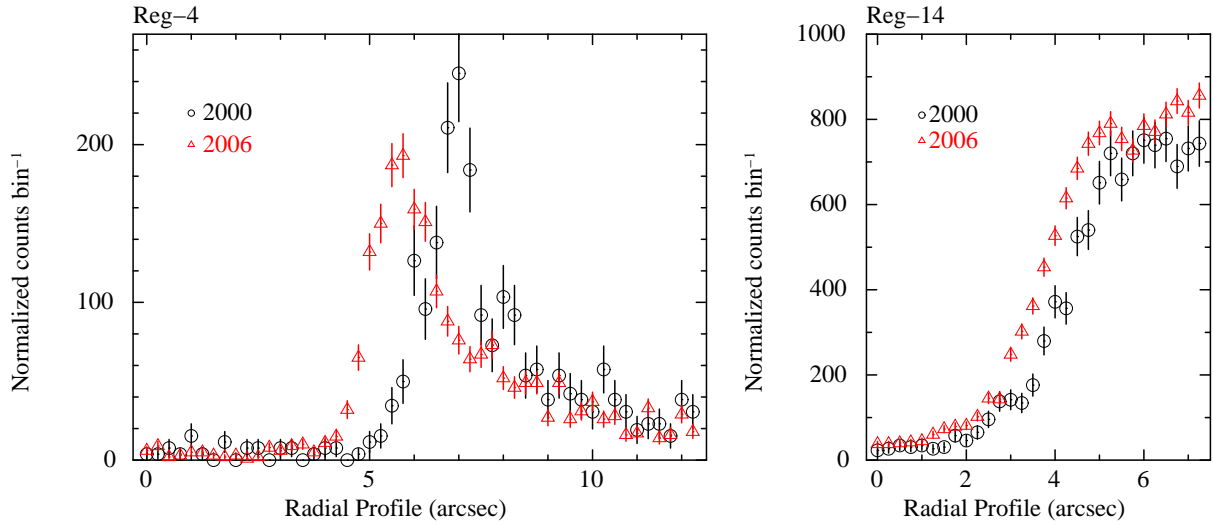


Fig. 2.— *Left*: Radial profiles binned with a $0''.25$ scale derived for Reg-4. Data points with circles and triangles represent the first- and the second-epoch observations, respectively. The shock motion is in the left direction. *Right*: Same as *left* but for Reg-14.

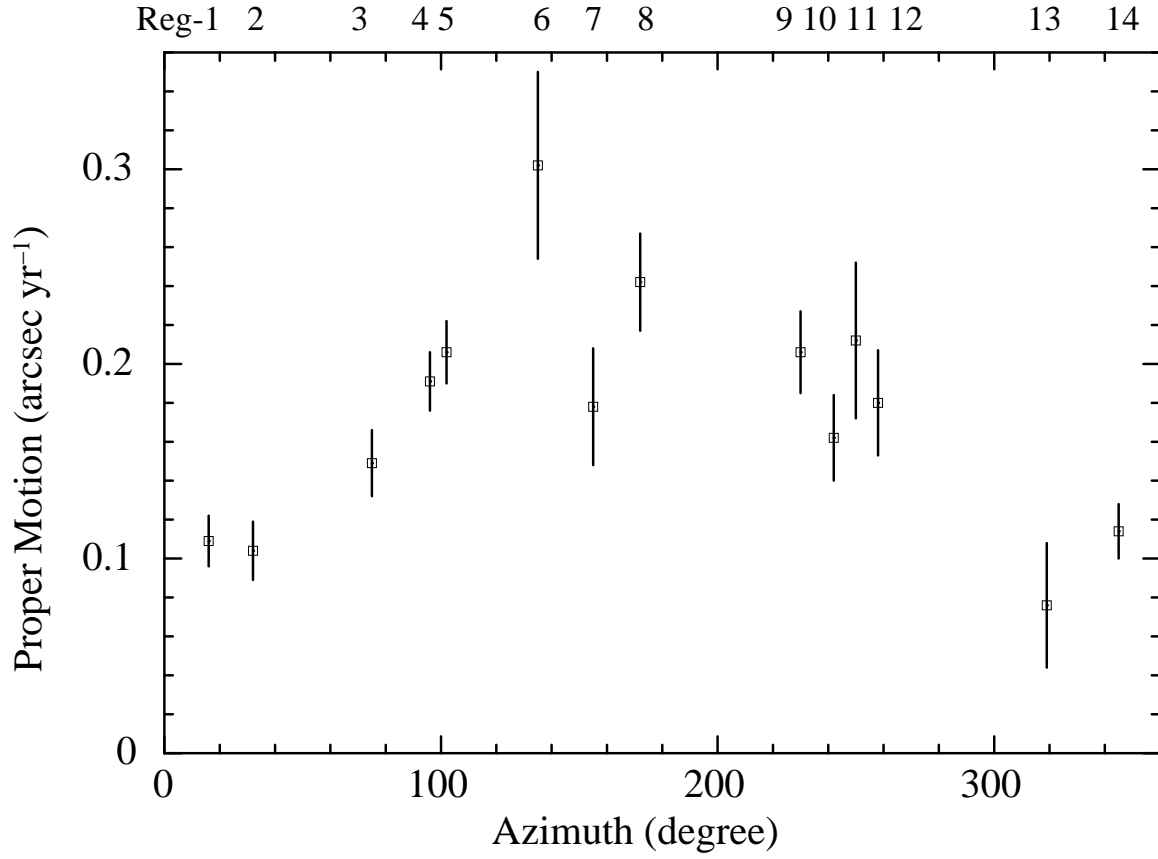


Fig. 3.— Proper motions as a function of azimuthal angle (lower x-axis) and region number (upper x-axis). Note that quoted errors represent only statistical uncertainties.

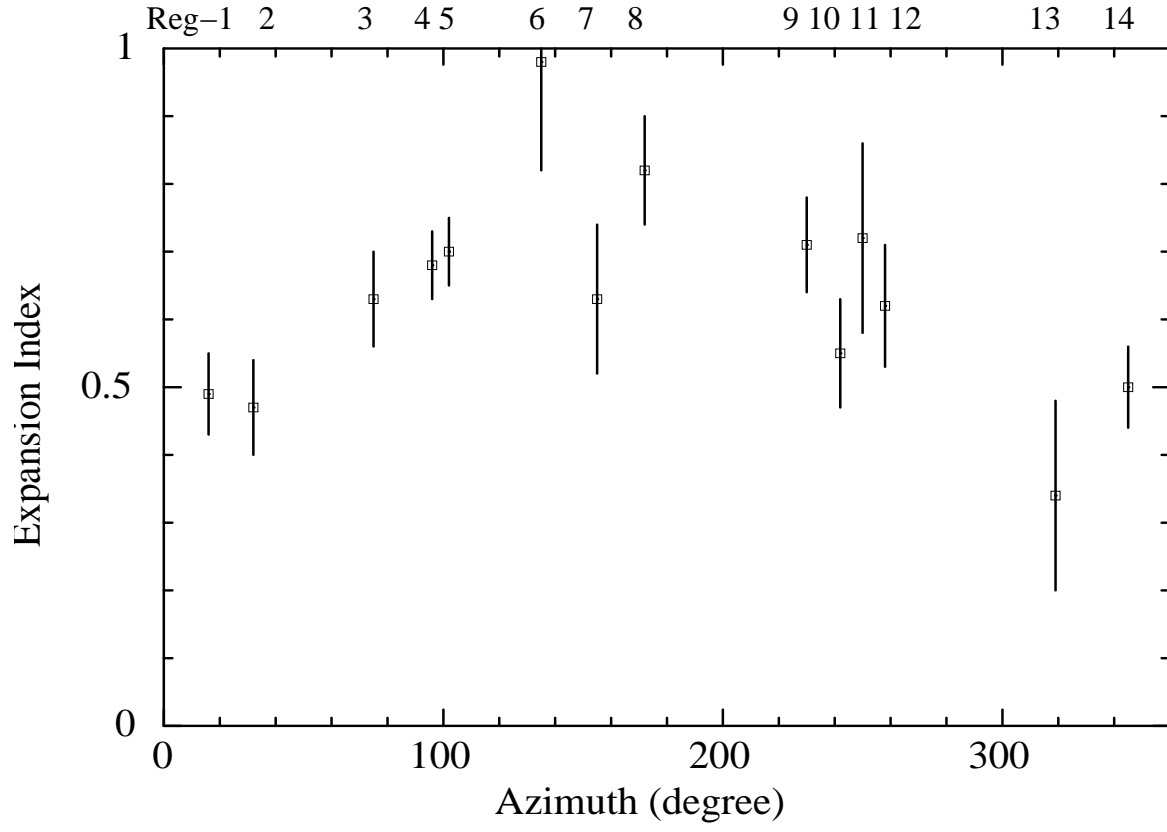


Fig. 4.— Same as Fig. 3 but for expansion indices.

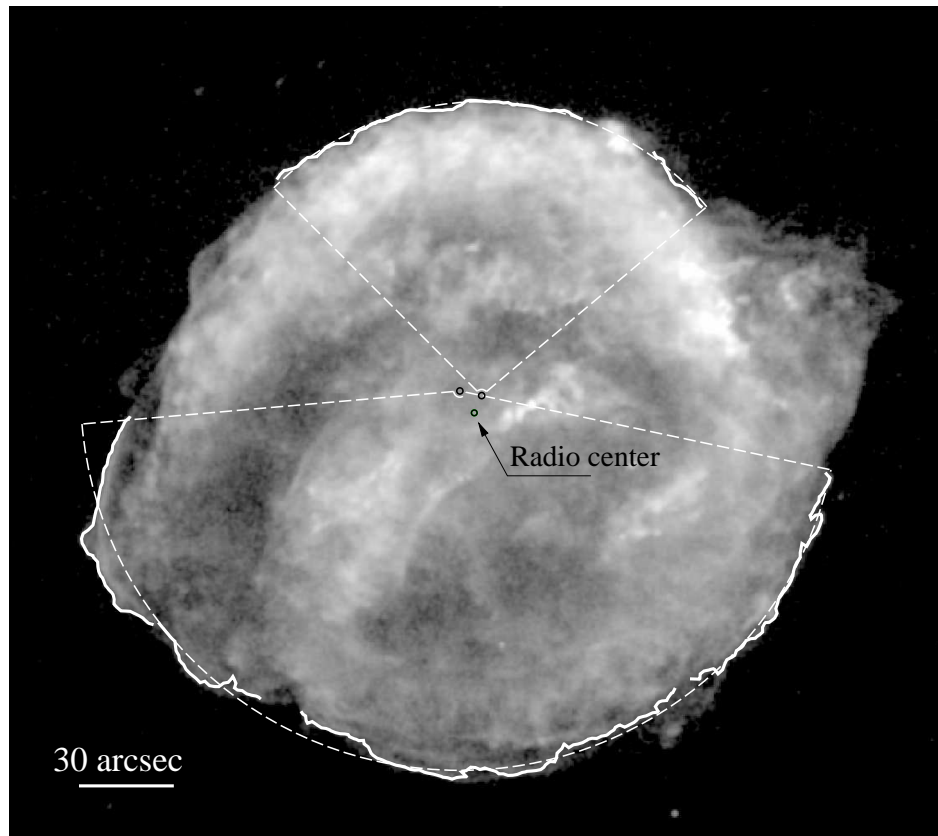


Fig. 5.— Best-fit circles to represent the X-ray boundaries of the northern and southern halves of the remnant are indicated as white dashed pie superposed on the second-epoch *Chandra* 0.3–8.0 keV band image. The radio center (Matsui et al. 1984) is also indicated as a small black circle. White contours (5 counts per pixel) are the X-ray boundaries used to estimate the best-fit circles shown in this image.

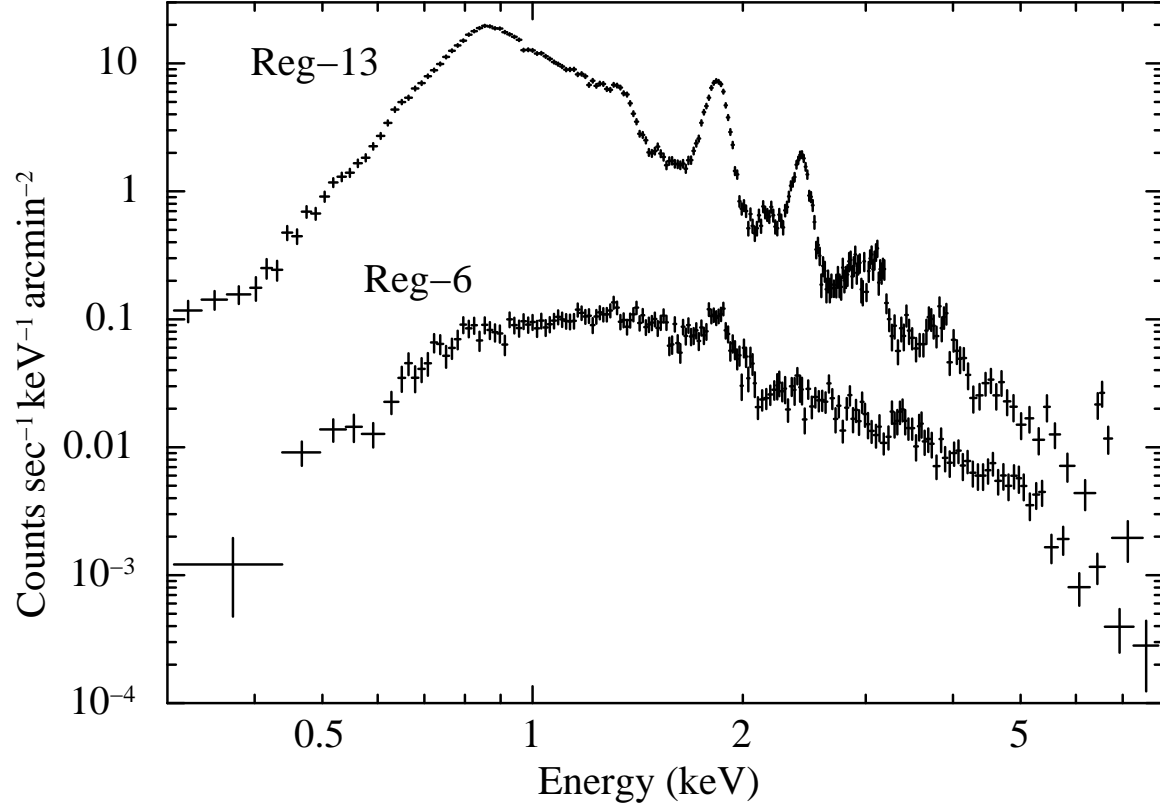


Fig. 6.— Spectra extracted from the southeastern rim around Reg-6 and the northwestern rim around Reg-13.